Direct Numerical Simulation of Particulate Flows Using a Fictitious Domain Method

Bircan Avci and Peter Wriggers

Abstract Multiphase flows consisting of a continuous fluid phase and a dispersed phase of macroscopic particles are present in many engineering applications. In general, a main task in the study of the particle-laden fluid flow of an application is to make predictions about the system's nature for various boundary conditions, since, depending on the volume fraction and mass concentration of the dispersed phase a fluid-particle system shows quite different flow properties. Unfortunately, often it is impossible to investigate such a system experimentally in detail or even at all. An option to capture and to predict its properties is performing a direct numerical simulation of the particulate fluid. For this purpose, a model approach based on a fictitious domain method is proposed in this contribution. Here, the fluid and the particle phase are treated, respectively, within the framework of the finite element method and the discrete element method. The coupling scheme, which accounts for the phase interaction, is realized at the particle scale. For the computation of the forces that the fluid exerts on a particle an approach is used in which they are determined directly from the flow field in the vicinity of its surface.

1 Introduction

Particulate flows are of great importance in very different industrial branches, e.g., in medical, process and chemical industries and also in geotechnical engineering and bioengineering. Examples include fluidized beds, sedimentation, fluvial erosion, sand production in oil wells, dust collection devices and aerosol transport in human respiratory airways. The characteristics involving particulate flows are up to now

B. Avci (✉) · P. Wriggers
Institute of Continuum Mechanics, Appelstrasse 11, 30167 Hannover, Germany
e-mail: avci@ikm.uni-hannover.de

P. Wriggers
e-mail: wriggers@ikm.uni-hannover.de

neither well-investigated nor well-understood, particularly with regard to flows with a dispersed phase composed of macroscopic particles. From the side of industry and applied sciences there exists an intense interest in understanding the processes taking place in these flows in order to predict their behavior, because a profound knowledge of the fluid-particle interaction would allow easily to improve the performance of an existing system or to design more efficient systems in the future; but the conduction of experiments on particulate flow systems—unless they can be carried out at all—is expensive and time-consuming. Performing virtual experiments on models via numerical simulations is of course an alternative way to gain some insight into the flow properties of a multiphase system. However, due to existing crucial limitations regarding the hardware technology and the scalability of algorithms, simulations cannot often totally replace real laboratory experiments. Thus, they are still required, but even so the knowledge extracted from representative small-scale virtual experiments can contribute in minimizing the sequence of real experiments. Consequently, the improvement of existing as well as the development of new frameworks for simulation of particulate flows is significant and demands more effort, as the simulation of problems with large number of particles is still a great challenging task.

In particle-laden multiphase flows the strength of the phase coupling is predominantly determined both by the local volume fraction of the dispersed phase and by its mass concentration (see, e.g., Crowe [11]). That means that in case of dense or locally highly concentrated flows the presence of particles in the fluid field can be a determining factor for the main characteristics inherent to an engineering system. To capture the mutual interaction of the phases in such flows, it is crucial to analyze the respective problem at the particle scale. This necessity implies a fully resolved model where the particles are described as having a body volume, and not just as point-particles, because in dense flows neighboring particles can interact not only via close range effects—like contact forces, adhesion or agglomeration—, but also via long range effects due to particle induced wakes, eddies and other local disturbances. Those effects can only be captured in the framework of a full 3D direct numerical simulation (DNS). However, a full 3D DNS approach requires very powerful techniques and is nontrivial, even when considering systems with only one immersed particle settling in a fluid, let alone systems with some thousands of dispersed particles in the fluid. This is due to the fact that besides the handling of the evolution of the time varying fluid domain, the motion of the fluid-particle boundaries needs to be continuously tracked during the flow process in order to account for the momentum exchanges taking place at the phase interfaces.

In the last two decades, great progress has been made in the development and improvement of DNS methods for particulate flow simulations. Basically, the proposed approaches may be classified into two groups: (i) adaptive grid methods and (ii) fixed grid methods. The first DNS approaches published in the literature are assigned to the category (i). Here, the fluid field is described using a body-fitted moving mesh whose elements follow locally the boundaries of the particles being in motion. Of course, depending on the particles' motion this can lead to large element distortions in a mesh, so that the grid needs to be re-meshed from time to time. Such a procedure is computationally very intensive, and one requires, in fact, very

efficient and sophisticated mesh motion and re-meshing algorithms. The first 3D DNS computations of particulate flows belonging to this category were presented in Johnson and Tezduyar [23], which can be considered as a pioneering work in this area (see also Johnson and Tezduyar [24–26]). In these articles, the authors propose the deformable-spatial-domain/stabilized space–time (DSD/SST) finite element method (FEM) setting for the treatment of the fluid field. Further milestone contributions related to group (i) were published by Hu et al. [19–21]. These authors employ in their work the Arbitrary-Lagrangian-Eulerian method framework in order to describe the particulate fluid field. In terms of the approaches assigned to the fixed-grid category (ii), one can find in the literature a number of techniques suggested for the DNS analysis of fluid-particle interactions (see the review paper of Haeri and Shrimpton [17] and the references cited therein for an overview). Taken together the proposed approaches are known under the generic term fictitious domain (FD) method. The most widely-used ones are the immersed boundary method, the distributed Lagrange multiplier/fictitious domain method and the fictitious boundary method. They all have in common that the fluid flow is treated in the framework of an Eulerian setting, where a fixed mesh is employed. Here, a fluid mesh covers, compared to the approaches in group (i), the whole computational domain, also including the space of the particles—that means the solid domain is filled as well with fluid. The main idea on which the FD methods are based is to uncouple the particles from the mesh and to consider them as fictitious objects having the property to traverse through the grid without causing any element deformation. The crucial point is here to enforce the fluid enclosed by an embedded particle to adopt its solid body motion. In general, this is realized through imposing additional implicit constraints to the flow field.

A prominent method to simulate granular materials is the well-established discrete element method (DEM) approach, which was proposed originally by Cundall and Strack [12]. The application of a DEM solver to predict the behavior of the dispersed phase in a particulate flow can be found, e.g., in Wachs [41] and Avci and Wriggers [3]. In a DEM setting, usually a soft sphere approach based on repulsive force models is applied in order to describe the contact among particles, which are at the same time assumed being quasi-rigid.

In this work, a DNS approach is developed in the framework of a FD strategy for the numerical simulation of 3D particle-laden flows. The fluid-particle interactions are computed at the particle scale, with a fully resolved flow around the particles. As numerical solvers regarding the simulation of the fluid part and particle part, the FEM and DEM are used, respectively. Here, both methods are appropriately coupled by a staggered solution procedure to handle particulate flows.

2 Governing Equations

A multiphase domain $\Omega \in \mathbb{R}^3$ is considered to describe a particulate fluid that consists of a flow field $\Omega_f(t)$ and N particles. Therein, each particle $\mathscr{P}_i$ occupies the domain $\Omega_p^i(t)$. Hence, for Ω it follows: $\Omega = \Omega_f(t) \cup \{\Omega_p^i(t)\}_{i=1,N}$.

The flow of the fluid field is modeled by the non-stationary incompressible Navier–Stokes equations:

$$\rho_f \left(\frac{\partial \mathbf{u}_f}{\partial t} + \mathbf{u}_f \cdot \nabla \mathbf{u}_f \right) - \nabla \cdot \boldsymbol{\sigma} = \mathbf{0}, \quad \nabla \cdot \mathbf{u}_f = 0, \quad \forall \mathbf{x} \in \Omega_f. \tag{1}$$

Herein, $\mathbf{u}_f$ is the fluid velocity, ρ_f the fluid density and $\boldsymbol{\sigma}$ describes the Cauchy stress tensor. In the numerical studies the constitutive equation for a Newtonian flow is used:

$$\boldsymbol{\sigma} = -p\mathbf{I} + 2\mu\boldsymbol{\varepsilon} \quad \text{with} \quad \boldsymbol{\varepsilon} = \frac{1}{2} \left(\nabla \mathbf{u}_f + (\nabla \mathbf{u}_f)^T \right), \tag{2}$$

where p is the pressure, $\mathbf{I}$ the identity tensor, μ the dynamic viscosity and $\boldsymbol{\varepsilon}$ the strain rate tensor.

The motion of a quasi rigid particle $\mathscr{P}$ can be deduced from the Newton–Euler equations. Consequently, its translational and angular velocities, $\mathbf{U} = \dot{\mathbf{X}}$ and $\boldsymbol{\omega}$, have to satisfy:

$$M \frac{d^2 \mathbf{X}}{dt^2} = (\rho - \rho_f) V \mathbf{b} + \mathbf{F} + \mathbf{F}_f \tag{3}$$

$$\boldsymbol{\theta} \frac{d\boldsymbol{\omega}}{dt} + \boldsymbol{\omega} \times (\boldsymbol{\theta}\boldsymbol{\omega}) = \mathbf{T} + \mathbf{T}_f. \tag{4}$$

Therein, M is the mass, $\mathbf{X}$ the position vector to the center of mass $\mathscr{M}$, ρ the mass density, $\mathbf{b}$ the gravity and V denotes the volume of $\mathscr{P}$. The tensor of inertia is represented by $\boldsymbol{\theta}$. Furthermore, the sum of the contact forces is stated as $\mathbf{F}$ and the fluid force that acts upon the particle surface $\partial \Omega_p$ is considered by $\mathbf{F}_f$. The torques that are caused by $\mathbf{F}$ and $\mathbf{F}_f$ with respect to $\mathscr{M}$ are associated to the quantities $\mathbf{T}$ and $\mathbf{T}_f$, respectively. Hence, the fluid forces can be obtained by:

$$\mathbf{F}_f = \int_{\partial \Omega_p} \mathbf{t} \, dA \quad \text{and} \quad \mathbf{T}_f = \int_{\partial \Omega_p} \mathbf{r} \times \mathbf{t} \, dA. \tag{5}$$

The traction vector $\mathbf{t}$ on $\partial \Omega_p$ is defined as $\mathbf{t} = \boldsymbol{\sigma}\mathbf{n}_f$, where $\mathbf{n}_f$ is the unit outward normal vector and $\mathbf{r}$ is the position vector of a point at $\partial \Omega_p$ with respect to $\mathscr{M}$.

3 Constitutive Modeling of the Particle Phase

The particles, which are immersed in the fluid, are modeled as quasi rigid spheres. To describe their collision behavior, a force-displacement based approach relying on repulsive models is used, which allows to determine the inter-particle forces. In the sections below, the relevant concepts of the contact models are stated briefly.

3.1 Normal Contact Model

The normal contact forces acting between colliding particles and between particles and system boundaries are described by a constitutive viscoelastic model. For adhesive particles being in contact, the JKR theory, introduced by Johnson et al. [27], is used to determine the resultant attractive van der Waals force F_a^n in the contact area (see also Maugis [35] for a detailed description of this model). As shown by Loskofsky et al. [31], the JKR theory yields even in the case of underwater adhesion satisfying results. For the purpose of governing the elastic contact force F_e^n, the Hertzian law [18] constitutes a well-established model. If the particles to be treated have also viscous material properties, for this, a consistent phenomenological model was presented in Brilliantov et al. [5, 6], where the effect of viscosity is considered via an added dissipative force F_d^n. Thus, one obtains for the forces acting on a particle:

$$F^n = F_e^n - F_a^n + F_d^n. \tag{6}$$

The elastic repulsive force based on the Hertzian contact law is determined by:

$$F_e^n = \frac{4}{3} E \sqrt{R} \, \delta^{3/2}, \tag{7}$$

where $\delta = \delta_i + \delta_j$ is the total particle compression, R and E are the effective radius and the effective Young's modulus of the contact pair $\mathscr{P}_i$ and $\mathscr{P}_j$, respectively (see Hertz [18]). As a result of the mutual compression of the particles, a circular area is formed in the contact zone. In the Hertz model, the radius a of this area, which is often called contact radius, is related to the total deformation δ via $a^2 = R\delta$.

According to the JKR model, it is implied that the adhesive force acts only within the contact area. Here, the work of adhesion to separate a unit contact area of $\mathscr{P}_i$ and $\mathscr{P}_j$ in a liquid medium (l) is defined as $W = \gamma_{il} + \gamma_{jl} - \gamma_{ij}$, where γ describes the respective interfacial energy (see, e.g., Loskofsky et al. [31]). Since the adhesive force F_a^n is opposed to the elastic force F_e^n, it reduces the elastic deformation δ_e, and one obtains for the total deformation:

$$\delta := \delta_e - \delta_a = \frac{a^2}{R} - \sqrt{\frac{2\pi \, W a}{E}}, \tag{8}$$

where the second term δ_a is due to adhesion (see, e.g., Maugis [35] for details). Based on this model the difference between the elastic and the adhesive force is given by:

$$F_{ea}^n := F_e^n - F_a^n = \frac{4 E a^3}{3R} - 2\pi a^2 \sqrt{\frac{2 W E}{\pi a}}. \tag{9}$$

A special case here is the situation when external forces are absent. If so, an equilibrium contact area with radius a_0 is formed in the contact zone due to the mutual

compression δ_0 of the particles caused just by their adhesive attraction. These both quantities are defined as:

$$a_0 = \left(\frac{9\pi\,W R^2}{2E}\right)^{1/3} \quad \text{and} \quad \delta_0 = \left(\frac{3R}{4}\left(\frac{\pi\,W}{E}\right)^2\right)^{1/3}. \tag{10}$$

To separate the particles, one has to apply a traction force under which they suffer minute stretching deformations forming a connecting neck around the contact zone. Once the pulling force has reached a critical level, i.e., $F^n = -F_c^n$, the contact breaks. Here, the critical force is obtained by $F_c^n = 3\pi\,W R/2$ and the corresponding critical deformation of the particle pair is $\delta_c = a_0^2/(48^{1/3}R)$. That means, the pulling distance regarding their detachment is defined as $\delta = -\delta_c$. By incorporating these critical quantities, one yields for the displacement δ in (8) and the force F_{ea}^n in (9) the following dimensionless relationships (see Chokshi et al. [9]):

$$\frac{\delta}{\delta_c} = 6^{1/3}\left[2\left(\frac{a}{a_0}\right)^2 - \frac{4}{3}\left(\frac{a}{a_0}\right)^{1/2}\right] \tag{11}$$

$$\frac{F_{ea}^n}{F_c} = 4\left(\frac{a}{a_0}\right)^3 - 4\left(\frac{a}{a_0}\right)^{3/2}. \tag{12}$$

To consider the properties of material viscosity, a dissipative force is adopted according to Brilliantov et al. [5]. In that work, the definition of the force is given as $F_d^n = A\dot{a}\,\partial F_{ea}^n/\partial a$. From this definition, the viscous force can be written as follows:

$$F_d^n = A\dot{a}\left(\frac{4Ea^2}{R} - \frac{3}{2}\sqrt{8\pi\,W E a}\right), \tag{13}$$

where the dissipative factor A is related to a constant function of material viscosity, which can also be used as a fitting parameter.

In the present contribution, the force laws on which F^n in (6) is based are algorithmically treated as displacement driven (see, e.g., Wriggers [43]). Introducing the penetration measure $g^n = (R_i + R_j) - ||\mathbf{X}_i - \mathbf{X}_j|| > 0$ and equating $g^n \equiv \delta$ as the mutual compression of $\mathscr{P}_i$ and $\mathscr{P}_j$, the individual parts of the force F^n can be computed straightforward after having determined the contact radius a. To evaluate this quantity, one has to solve the nonlinear expression in (11) for the currently calculated penetration δ of the examined pair of particles. The direction of the contact force $\mathbf{F}^n = F^n\mathbf{n}$ of the respective particle is opposed to the direction of its displacement, where $\mathbf{n} = (\mathbf{X}_i - \mathbf{X}_j)/||\mathbf{X}_i - \mathbf{X}_j||$ is the normal unit vector pointing from $\mathscr{M}_j$ towards $\mathscr{M}_i$.

3.2 Tangential Contact Model

The constitutive relation of Coulomb's law couples the tangential force F^t via the coefficient of friction to the normal force F^n such that the relation $F^t = \mu_d F^n$ holds for sliding and $F^t \leq \mu_s F^n$ for sticking. Therein, the dynamic and the static friction coefficients are denoted by μ_d and μ_s, respectively, where $\mu_d \leq \mu_s$. For a constitutive treatment of F^t, a classical tangential (linear) spring-dashpot element with an incorporated slider is used in this work in order to model the tangential friction problem. For an overview and a discussion of different tangential contact models proposed in the literature in the context of the DEM see Kruggel-Emden et al. [28]. Here, a return mapping scheme is adopted for the computation of the tangential force (see Luding [32], Wriggers [43]). This projection method needs a tangential trail traction that takes the form:

$$\mathbf{F}_o^t = -(c^t \mathbf{g}^t + d^t \mathbf{v}^t). \tag{14}$$

Therein, $\mathbf{g}^t$ is the elongation of the tangential spring, c^t and d^t are the tangential spring stiffness and the tangential dissipation parameter, respectively. The tangential relative velocity at the contact point $\mathscr{C}$ is given by $\mathbf{v}^t = \mathbf{v}^s - (\mathbf{v}^s \cdot \mathbf{n})\,\mathbf{n}$ with $\mathbf{v}^s = \mathbf{v}_i^{\mathscr{C}} - \mathbf{v}_j^{\mathscr{C}}$ as the relative velocity at $\mathscr{C}$, where the corresponding local velocities are defined by $\mathbf{v}_i^{\mathscr{C}} = \mathbf{U}_i + \boldsymbol{\omega}_i \times \mathbf{r}_i$ and $\mathbf{v}_j^{\mathscr{C}} = \mathbf{U}_j + \boldsymbol{\omega}_j \times \mathbf{r}_j$. The vectors pointing from $\mathscr{M}_i$ and $\mathscr{M}_j$ to $\mathscr{C}$ are associated with $\mathbf{r}_i = R_i(-\mathbf{n})$ and $\mathbf{r}_j = R_j \mathbf{n}$, respectively. By introducing a trial function f^{tr}, the following relation can be stated for the tangential contact:

$$f^{\mathrm{tr}} := ||\mathbf{F}_o^t|| - \mu_s ||\mathbf{F}^n|| \Rightarrow \begin{cases} \leq 0 \;:\; \text{stick} \\ > 0 \;:\; \text{slip}. \end{cases} \tag{15}$$

If $f^{\mathrm{tr}} \leq 0$, the contact point $\mathscr{C}$ is in the stick region, and if $f^{\mathrm{tr}} > 0$, it is in the slip region. In the latter case, sliding occurs in the contact area. Note that if $F_o^t < \mu_d F^n$ becomes valid during a sliding process, then the stick case comes into effect. If the contact point sticks within the current time step, the actual tangential spring $\mathbf{g}^t$ is incremented for the succeeding time step by the relation $\Delta \mathbf{g}^t = \mathbf{v}^t \Delta t_{\mathrm{D}}$. Consequently, the new spring length is defined by $\bar{\mathbf{g}}^t = \mathbf{g}^t + \Delta \mathbf{g}^t$. Here, Δt_{D} denotes the time step size of the DEM. But if the contact point slides within the time step, then the tangential spring is adjusted by means of:

$$\bar{\mathbf{g}}^t = -\frac{1}{c^t}(\mu_d F^n \mathbf{t} + d^t \mathbf{v}^t) \tag{16}$$

in order to fulfill the Coulomb's slip condition. Therein, $\mathbf{t} = \mathbf{F}_o^t / ||\mathbf{F}_o^t||$ is the direction of the trial traction. In two subsequent time steps, the contact area might be slightly rotated. To take this into account, one can—as proposed in Luding [32]—project the tangential spring onto the current rotated contact area at the beginning of each new time step via $\mathbf{g}^t = \bar{\mathbf{g}}^t - (\bar{\mathbf{g}}^t \cdot \mathbf{n})\mathbf{n}$. Finally, in the context of the return mapping

scheme, the tangential contact force is $F^t = ||\mathbf{F}_o^t||$ if $f^{\text{tr}} \leq 0$ holds and $F^t = \mu_d F^n$ if $f^{\text{tr}} > 0$. By computing F^t, one obtains $\mathbf{F}^t = F^t \mathbf{t}$ and $\mathbf{T}^t = \mathbf{r} \times \mathbf{F}^t$ that contributes to $\mathbf{F}$ and $\mathbf{T}$ in (3) and (4), respectively.

3.3 Rolling Resistance Model

During a rolling motion of two particles the leading part of the contact area is continuously compressed and the trailing part is decompressed with respect to the rolling direction. In case of an attractive van der Waals force in the contact area, the particles suffer an opposing torque that generates rolling resistance. Here, a model consisting of a rolling spring-dashpot-slider element is adopted (see Iwashita and Oda [22]). At this, the opposing torque is given by:

$$\mathbf{M}_o^r = -(c^\phi \boldsymbol{\phi} + d^\phi \dot{\boldsymbol{\phi}}).$$ (17)

Therein, c^ϕ is the rolling stiffness, d^ϕ the rolling viscosity coefficient, $\boldsymbol{\phi}$ the relative particle rotation and $\dot{\boldsymbol{\phi}}$ denotes the corresponding relative rotational velocity. By introducing a trial force $\mathbf{F}_o^r$ that induces an equivalent torque to $\mathbf{M}_o^r$, the problem of rolling resistance can be treated algorithmically like the model of tangential friction (see Luding [33]). In this regard, the equivalent formulation can be stated as follows:

$$\mathbf{M}_o^r = R\,\mathbf{n} \times \mathbf{F}_o^r,$$ (18)

with $\mathbf{F}_o^r = -(c^\xi\,\mathbf{g}^r + d^\xi\,\mathbf{v}^r), c^\xi = c^\phi/R^2$ and $d^\xi = d^\phi/R^2$. Here, $\mathbf{g}^r$ is the elongation of the spring and $\mathbf{v}^r$ denotes the rolling velocity that can be computed according to Kuhn and Bagi [29] using:

$$\mathbf{v}^r = -R\Big[(\boldsymbol{\omega}_i - \boldsymbol{\omega}_j) \times \mathbf{n} - \frac{1}{2}\Big(\frac{1}{R_j} - \frac{1}{R_i}\Big)\mathbf{v}^t\Big].$$ (19)

Assuming that the slider can sustain a certain critical rolling resistance torque M_c^r, one can write analog to (15):

$$f_r^{\text{tr}} := ||\mathbf{F}_o^r|| - \frac{M_c^r}{R} \Rightarrow \begin{cases} \leq 0 : \text{ stick } \Rightarrow & F^r = ||\mathbf{F}_o^r|| \\ > 0 : \text{ slip } \Rightarrow & F^r = M_c^r/R. \end{cases}$$ (20)

With regard to the numerical handling of the spring in this context, the respective relationships can be expressed in a summarized form as:

$$f_r^{\text{tr}} := \begin{cases} < 0 \Rightarrow \bar{\mathbf{g}}^r = \mathbf{g}^r + \Delta\mathbf{g}^r, & \Delta\mathbf{g}^r = \mathbf{v}^r \Delta t \\ > 0 \Rightarrow \bar{\mathbf{g}}^r = -\dfrac{1}{c^\xi}\Big[F_c^r\,\mathbf{t}^r + d^\xi\,\mathbf{v}^r\Big], & \mathbf{t}^r = \dfrac{\mathbf{F}_o^r}{||\mathbf{F}_o^r||}, \ F_c^r = \dfrac{M_c^r}{R}. \end{cases}$$ (21)
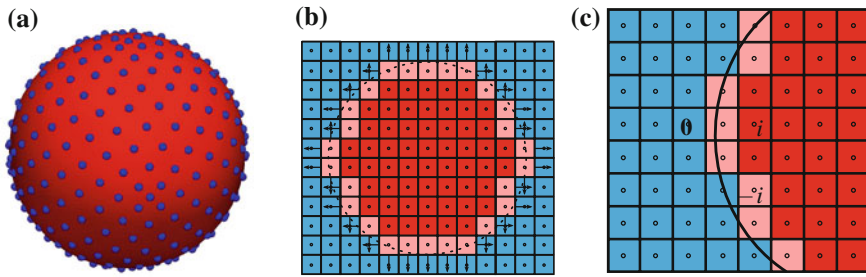
Fig. 1 **a** Distribution of the Lebedev quadrature points for the case of $N_L = 302$ points. **b** Steplike discretization of a particle for the evaluation of fluid forces. **c** A detail of the domain Ω showing the classification of computational elements

In this model, the projection direction of the spring relies on the common rolling direction of the pair of particles being in contact. Thus, the projection condition is defined as $\mathbf{g}^r = (\overline{\mathbf{g}}^r \cdot \tilde{\mathbf{t}}) \, \tilde{\mathbf{t}}$, where $\tilde{\mathbf{t}} = \mathbf{v}^r / ||\mathbf{v}^r||$. By computing F^r, one yields the pseudo force $\mathbf{F}^r = F^r \, \mathbf{t}^r$ and respectively the rolling resistance torque $\mathbf{M}^r = R\mathbf{n} \times \mathbf{F}^r$. Finally, the torques for the examined pair of particles $\{\mathscr{P}_i, \mathscr{P}_j\}$ can be written as follows: $\mathbf{M}_i^r = -\mathbf{M}_j^r =: \mathbf{M}^r$.

4 Phase Coupling

In the fixed grid approach, the mesh of the flow field does not coincide with the boundaries of the particles. Hence, information between the Eulerian and Lagrangian description has to be transferred. A further challenging issue concerning the coupling of the phases is the computation of the fluid forces acting on the particle surfaces.

4.1 Evaluation of the Fluid Forces

A crucial point regarding the study of fluid-particle interactions in a fully resolved 3D DNS framework is the computation of the fluid forces to which the immersed particles are subjected. To carry out this task, two different strategies, as shown in Fig. 1a, b, have been considered in this work. In the following, the approach illustrated in (a) should be abbreviated as AP1 and the one in (b) as AP2.

Approach AP1 For the integration of the fluid forces acting on the surface of a particle a quadrature rule can be used that was developed in Lebedev and Laikov [30]. In Fig. 1a, the distribution of the Lebedev integration points, which can also be seen as Lagrangian force points, is displayed for the case of $N_L = 302$ points. This numerical integration applied to particle $\mathscr{P}_i$ yields:

$$\mathbf{F}_f^i = \int_{\partial\Omega_p^i} \mathbf{t}\, d\mathrm{A} = \sum_{k=1}^{N_L} (d\mathbf{F})_k = J \sum_{k=1}^{N_L} w_k \mathbf{t}_k \tag{22}$$

$$\mathbf{T}_f^i = \int_{\partial\Omega_p^i} \mathbf{r} \times \mathbf{t}\, d\mathrm{A} = \sum_{k=1}^{N_L} \mathbf{r}_k \times (d\mathbf{F})_k = J \sum_{k=1}^{N_L} \mathbf{r}_k \times w_k \mathbf{t}_k. \tag{23}$$

Therein, $\mathbf{t}_k = (\langle\boldsymbol{\sigma}\rangle\mathbf{n})_k$ is the traction vector at the kth Lebedev point, w_k the corresponding integration weight and $\langle\boldsymbol{\sigma}\rangle = (1/V)\int \boldsymbol{\sigma}\, dV$ specifies the averaged fluid stress tensor of the finite element with volume V in which the point k is located. The mapping from a unit sphere to $\mathscr{P}_i$ is performed via the relation $J = 4\pi R_i^2$, where R_i is the particle radius.

Approach AP2 In this approach to the evaluation of the fluid forces exerting on $\mathscr{P}_i$, the shape of the particle surface is reproduced on the basis of the computational grid, see Fig. 1b. Here, the calculation of $\mathbf{F}_f^i$ and $\mathbf{T}_f^i$ is carried out using the steplike reconstructed surface contour of $\mathscr{P}_i$. To determine these forces from this surface, one has to compute the averaged tractions on the respective element faces $\overline{\Gamma}_j \{j = 1, \ldots, N_\Gamma\}$, and subsequently the corresponding forces can simply be summed up yielding:

$$\mathbf{F}_f^i = \int_{\partial\Omega_p^i} \mathbf{t}\, d\Gamma = \sum_{j=1}^{N_\Gamma} (d\mathbf{F})_j = \sum_{j=1}^{N_\Gamma} \mathbf{t}_j \overline{\Gamma}_j \tag{24}$$

$$\mathbf{T}_f^i = \int_{\partial\Omega_p^i} \mathbf{r} \times \mathbf{t}\, d\Gamma = \sum_{j=1}^{N_\Gamma} \mathbf{r}_{\Gamma_j} \times (d\mathbf{F})_j = \sum_{j=1}^{N_\Gamma} \mathbf{r}_{\Gamma_j} \times \mathbf{t}_j \overline{\Gamma}_j, \tag{25}$$

where $\mathbf{r}_{\Gamma_j}$ is the position vector of the center of the element surface $\overline{\Gamma}_j$ with respect to $\mathscr{M}_i$.

Remark To characterize the motion of the DEM particles sliding through the mesh, the mesh elements are labeled as depicted in Fig. 1c. By using the position of the element center point $\mathscr{E}$ as an assignment criteria, the elements that coincide with a particle domain Ω_p^i are marked at each time step by the particle number of $\mathscr{P}_i$. Here, the interior and boundary elements are defined by 'i' and '$-i$', respectively. Furthermore, fluid elements are denoted by '0'.

4.2 Coupling Constraints

For the coupling process, the rigid body motion of the particles is imposed on the flow field. The rigidity constraints due to $\mathscr{P}_i$ that are applied to the Navier–Stokes

equations can be regarded as additional Dirichlet no-slip boundary conditions (see, e.g., Wan and Turek [42]). The constraint for an interior velocity node $\mathscr{V} \in \Omega_p^i$ of an boundary element ' $-i$ ' is given by:

$$\mathbf{u}_f = \mathbf{U}_i + \boldsymbol{\omega}_i \times \mathbf{r}_p, \tag{26}$$

where $\mathbf{r}_p$ is the vector pointing from $\mathscr{M}_i$ to the considered velocity node. However, for a velocity node $\mathscr{V} \in \Omega_p^i$ that adjoins the fluid phase, the velocity constraint is defined as:

$$\mathbf{u}_f = (1 - \phi_A)\mathbf{u}_f + \phi_A(\mathbf{U}_i + \boldsymbol{\omega}_i \times \mathbf{r}_p), \tag{27}$$

where ϕ_A is the element face area fraction situated within Ω_p^i. Hence, ϕ_A acts as a weighting factor for $\mathscr{V}$.[1] But if $\mathscr{V} \notin \Omega_p^i$, then a nonlinear weighted strategy is applied according to Luo et al. [34], which reads:

$$\mathbf{u}_f = (1 - \phi_R)\mathbf{u}_f + \phi_R(\mathbf{U}_i + \boldsymbol{\omega}_i \times \mathbf{r}_p), \tag{28}$$

where the interpolation factor $\phi_R = e^{-Re_p|\alpha|}$ is a nonlinear function of the relative Reynolds number $Re_p = \rho_f||\mathbf{U}_i - \mathbf{u}_f||D_i/\mu_f$ and of the relative distance $\alpha = h/D_i$. Here, D_i and h denote the particle diameter and the distance from $\mathscr{V}$ to the surface of $\mathscr{P}_i$, respectively.

5 Solution Algorithms

5.1 FEM Solver for the Fluid Problem

A spatial and temporal discretization of (1) yields a set of nonlinear algebraic equations for the fluid velocity $\mathbf{u}_f$ and the pressure $\mathbf{p}$. The resulting coupled equation system, which has to be solved at each time step, can be written as follows:

$$\begin{bmatrix} \mathbf{M} + \theta_1\Delta t \mathbf{N}(\mathbf{u}_f^{n+1}) & \theta_2\Delta t \mathbf{G} \\ \mathbf{G}^T & 0 \end{bmatrix} \begin{bmatrix} \mathbf{u}_f^{n+1} \\ \mathbf{p}^{n+1} \end{bmatrix} = \begin{bmatrix} (\mathbf{M} - \theta_3\Delta t \mathbf{N}(\mathbf{u}_f^n)) \, \mathbf{u}_f^n \\ 0 \end{bmatrix}. \tag{29}$$

Therein, $\mathbf{M}$ is the mass matrix, $\mathbf{N}$ the matrix including the diffusive, convective and stabilization terms, $\mathbf{G}$ the gradient matrix, $\mathbf{G}^T$ the divergence matrix, Δt the current time-step size and θ_{1-3} are parameters of the fractional step θ-scheme, see Turek

---

[1] In the present work, the nonconforming rotated trilinear $\tilde{Q}_1/Q_0$ element pair is used where a nodal value at $\mathscr{V}$ is the mean value of the velocity vector over the respective element face area, see Turek [38] for details. The velocity nodes of this element are located at the midpoints of the element faces.

[38] for details. To solve (29), the multigrid FEM solver FEATFLOW [39] is applied in this contribution.

5.2 DEM Solver for the Particle Problem

The movement of the particles is governed by the equations of motions given in (3) and (4). With regard to the numerical integration of these equations in time, the finite difference based Gear predictor–corrector scheme of third and fourth order is applied. The Gear integration scheme is subdivided into three steps: (1) prediction of all the kinematic variables, (2) evaluation of the forces according to Sect. 3 by using the predicted variables and, subsequently, computation of the corresponding accelerations and, finally, (3) correction of the predicted kinematic variables based on the new accelerations. For the algorithmic details of the Gear scheme see Allen and Tildesley [1].

Remark An aspect that has also to be considered in the framework of developing a FEM-DEM coupling scheme is the widely differing computational time scale between the both numerical methods. Since, due to the displacement driven character of the DEM concerning the force computation, one usually has $\Delta t_D \ll \Delta t$. To handle this problem of unequal time scales, a sub cycling strategy can be used as suggested by Feng et al. [13].

5.3 Search Algorithms

The computation of the contact forces is the most CPU time consuming part of a DEM simulation. Here, the evaluation of the contact detection has to be minimized to the neighbors of a particle, since they are its only relevant potential contact partners. For this purpose, the Verlet-List and the Linked-Cell is combined in order to yield a fast contact search algorithm (see, e.g., Allen and Tildesley [1], Pöschel and Schwager [36]).

In the Verlet-List procedure a list of neighboring particle indices is maintained for each particle in the system. By defining a Verlet distance threshold value v_d, a pair of particles can be considered as neighbor if $v_d > |g^n|$ holds. Once the Verlet-List is built, the contact detection needs only to be evaluated for the neighboring pairs. As a result, this task scales with respect to the corresponding computational effort with $O(N)$. Certainly, the list has to be updated at some intervals. In this regard, a possible rebuild criteria can be defined by $\Delta s_{max} \geq 0.6 v_d$, where Δs_{max} is the largest displacement of a particle since the last list update (see Pöschel and Schwager [36]). But the construction of the list in a straightforward manner scales with $O(N^2)$, thus, one has to speed up this task in order to obtain a search algorithm that scales in toto with $O(N)$. For this purpose, the computational domain is divided into cubic cells of uniform edge lengths where the cells are slightly larger than the largest particle in

the system. After assigning all particles to the cells relative to their center of mass, the relevant particles for the construction of the neighbor list of $\mathscr{P}_i$ are those who are referenced to the group of 27 cells consisting of the owner cell of $\mathscr{P}_i$ and of its direct 26 surrounding cells.

For a fast assignment of the element flags and, furthermore, in order to localize efficiently the elements containing the integration points for the computation of the fluid forces on the particles, the approach of the Linked-Cell method is used analogously. The Linked-Cell algorithm generates in this case an element list referring to the same cell structure as for the particles. Here, an element is referenced to a cell with respect to the position of the elements center point $\mathscr{E}$. Consequently, for the application of the velocity constraints related to particle $\mathscr{P}_i$ and for the computation of its fluid forces, only the elements are significant that are binned into the group of those 27 cells which are relevant for $\mathscr{P}_i$. In order to reduce the trial computations, some elements can also be excluded in advance from detailed considerations if the distance between $\mathscr{E}$ and $\partial\Omega_p^i$ is larger than a threshold value that can be chosen according to the largest element size in the computational domain.

6 Numerical Simulations

The numerical results of three computed test problems obtained by the presented approach are discussed next. The first test problem is the sedimentation of one particle in a box. In the second simulation example, the sedimentation of two particles in a row is considered in order to mimic their *drafting-kissing-tumbling* effect, and the last example deals with a particle-laden flow through a tube with changing cross section.

6.1 Sedimentation of a Single Particle in a Box

In this example, the sedimentation of a single particle in a box filled with fluid is examined. The considered system is shown in Fig. 2. This system corresponds to the setup that was experimentally investigated in ten Cate et al. [37] where the authors measured the settling velocity of the immersed particle under the action of gravity in four test cases, each with a different fluid. In the following, the obtained simulation results for the cases with minimum and maximum terminal particle Reynolds numbers, $Re_p = 1.5$ and $Re_p = 31.9$, are presented. Previously, the sedimentation problem of ten Cate et al. [37] was computed by, among others, Veeramani et al. [40] and Feng and Michaelides [14].

To discretize the box in Fig. 2, a uniform mesh consisting of 819,200 $\tilde{Q}_1/Q_0$ elements ($80 \times 80 \times 128$ elements) is used. All the simulations were carried out by imposing no-slip velocity conditions at the box boundaries. The diagrams in Fig. 3 show the computed temporal evolutions of the settling velocity of the particle
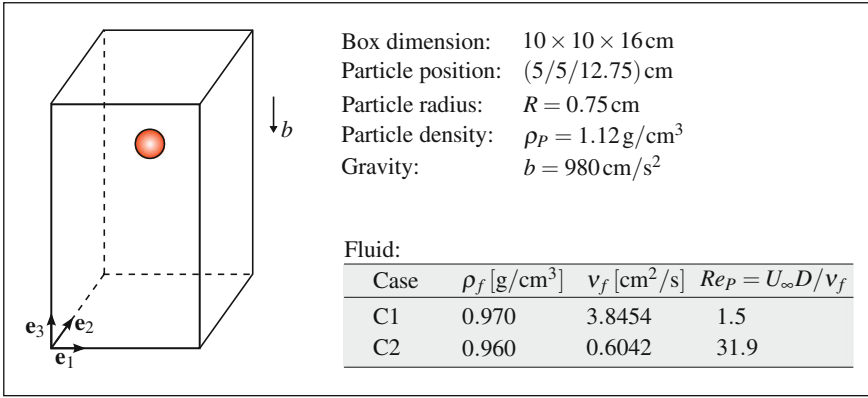
Box dimension:	$10 \times 10 \times 16$ cm
Particle position:	$(5/5/12.75)$ cm
Particle radius:	$R = 0.75$ cm
Particle density:	$\rho_P = 1.12$ g/cm^3
Gravity:	$b = 980$ cm/s^2

Fluid:

Case	ρ_f [g/cm^3]	ν_f [cm^2/s]	$Re_P = U_\infty D / \nu_f$
C1	0.970	3.8454	1.5
C2	0.960	0.6042	31.9

Fig. 2 Sedimentation of a single particle in a box. Geometry and material data
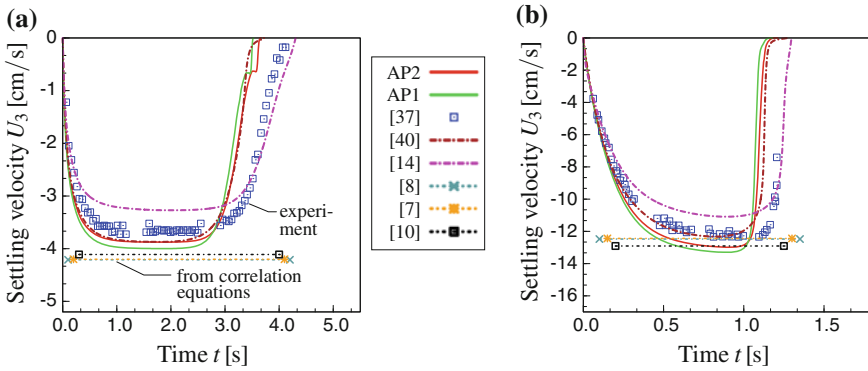
Fig. 3 Evolution of the settling velocity of the particle for **a** case C1 and **b** case C2

center in the direction of gravity for the considered two cases. As it can be seen, each case was simulated both by means of approach AP1 and AP2. Every diagram also includes the predicted terminal velocity of the particle based on the correlation equations[2] suggested in Clift et al. [10], Brown and Lawler [7] and Cheng [8], and furthermore, the numerical results of Veeramani et al. [40] and those of Feng and Michaelides [14]. At the beginning of the experiment, the particle is at rest, and it accelerates due to the action of gravity. It is observed that when the gravitational and the drag forces reach a state of equilibrium, the particle will sediment with a uniform velocity, which is called terminal velocity. The simulation results show that the presented model, both based on AP1 and AP2, is capable to predict the evolution of the particle's settling velocity. The maximum discrepancy of the predictions with

---

[2] In general, correlations for drag and terminal settling velocity are valid for a particle in an infinite domain, but they still provide reasonable results for a relatively large distance between a particle and system boundaries.
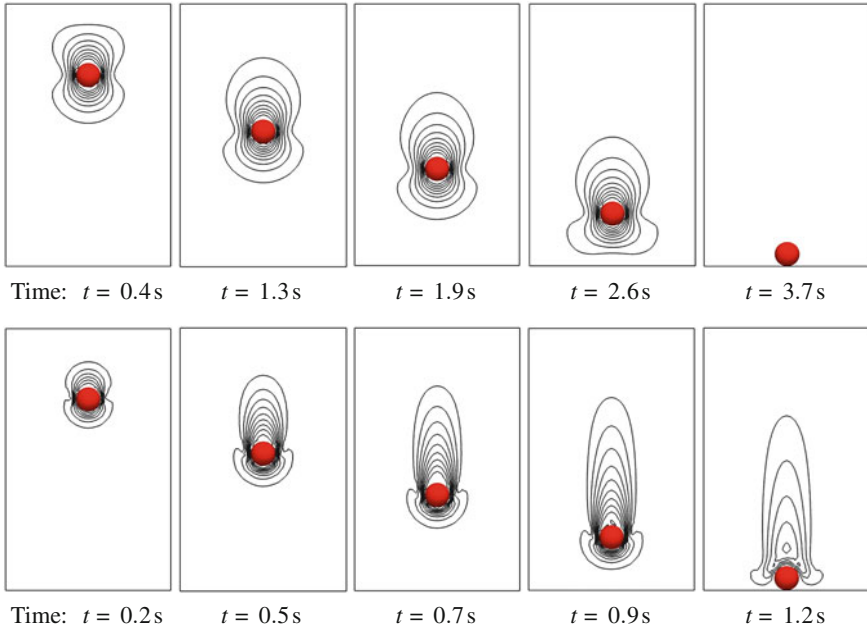
Time: $t = 0.4\,\mathrm{s}$ $t = 1.3\,\mathrm{s}$ $t = 1.9\,\mathrm{s}$ $t = 2.6\,\mathrm{s}$ $t = 3.7\,\mathrm{s}$

Time: $t = 0.2\,\mathrm{s}$ $t = 0.5\,\mathrm{s}$ $t = 0.7\,\mathrm{s}$ $t = 0.9\,\mathrm{s}$ $t = 1.2\,\mathrm{s}$

Fig. 4 Contour plots of the normalized velocity magnitude in the symmetry plane at different points in time. The plots of the *upper row* belong to case C1 and those of the *lower row* to case C2

respect to the experimental data is less than 8 %. In addition, the obtained results are in a very good agreement with those of Veeramani et al. [40], but there is a small mismatch compared with the results of Feng and Michaelides [14]. Figure 4 shows the computed contour plots of the normalized velocity magnitude $||\mathbf{u}_f||/U_\infty$ in the symmetry plane. Accordingly, the depicted contours range between 0 and 1. Here, an equal spacing of 0.1 is chosen. It shows that these plots agree well with those of ten Cate et al. [37], and that the presented model is well suited to mimic their sedimentation experiments. There is also a good agreement with the computed plots given in Apte et al. [2].

6.2 Sedimentation of Two Particles in a Box

This benchmark simulation is carried out to reproduce the *drafting-kissing-tumbling* effect of two particles sedimenting in a row, as it can be observed in laboratory experiments (see, e.g., the experiment reported in Fortes et al. [15]). Figure 5 shows the system with the particles being studied in this benchmark test. The depicted setup has been already numerically investigated by Glowinski et al. [16], Apte et al. [2] and Breugem [4]. For the discretization of the computational domain a uniform mesh of 1,048,576 $\tilde{Q}_1/Q_0$ elements ($64 \times 64 \times 256$ elements) is used. It is assumed that
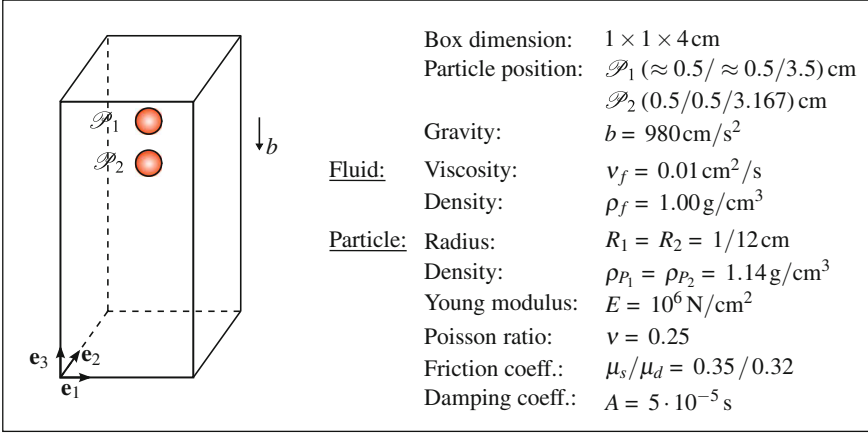
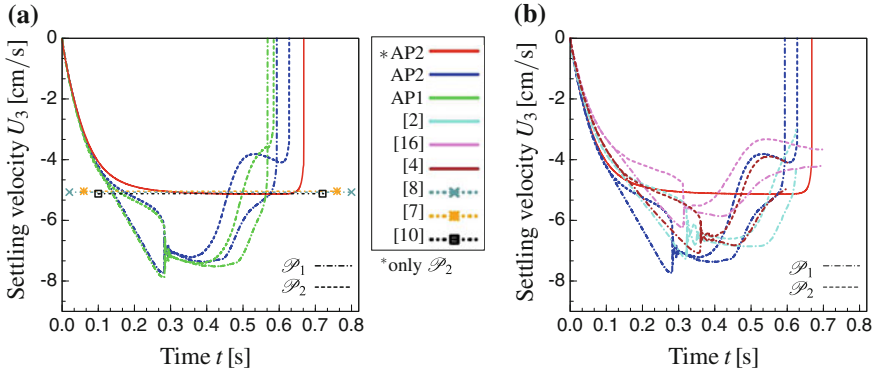Fig. 5 Sedimentation of two particles in a box. Geometry and material data

Fig. 6 Evolution of the settling velocities of the particles for the drafting-kissing-tumbling problem: **a** results of the present work and **b** comparison of the results with the literature

the box is fully filled with fluid. Concerning the boundary conditions of the fluid domain, no-slip velocity conditions are applied at the box walls. In order to provoke that the particles tumble when they kiss each other, a slight initial horizontal offset in the position of $\mathscr{P}_1$ is introduced such that $(0.5075/0.5075/3.5)$ cm. This offset is here necessary, because the numerical results of previous test computations based on different uniform symmetric meshes showed that the implemented algorithm maintains nearly the complete symmetric properties of the system. Thus, the flow field features too weak lateral disturbances in order to trigger the tumbling case (as if, for instance, a free or just an anisotropic mesh is used).

In order to verify that the numerical model is able to predict the terminal settling velocity of an almost undisturbed sedimenting single particle within the frame of this benchmark setup, the sedimentation of $\mathscr{P}_2$ was computed in advance without
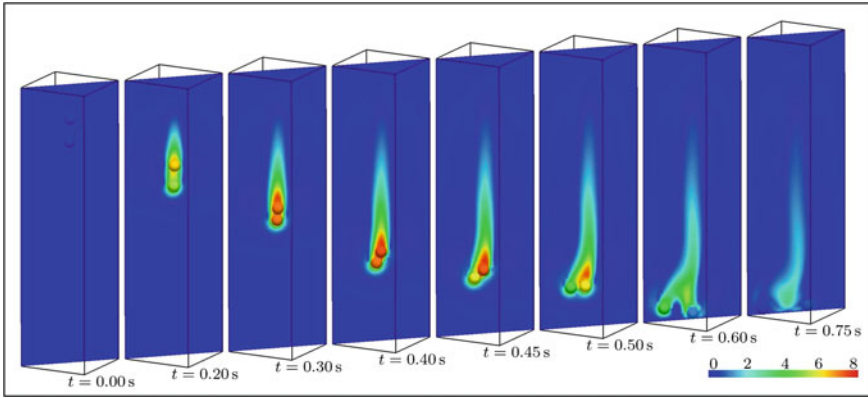
Fig. 7 Numerical results of the drafting-kissing-tumbling simulation at eight points in time

the presence of $\mathscr{P}_1$. Figure 6a shows the obtained time history of the falling velocity by using AP2, and one can see that the predicted terminal velocity matches those obtained with correlations. This diagram contains also the computed evolutions of the particle velocities by employing the approaches AP1 on the one hand and AP2 on the other hand for the *drafting-kissing-tumbling* case. It can be observed that the results obtained for both simulations agree quite well. With regard to a further verification of the presented algorithm and of its implementation, the predictions of AP2 are compared to other numerical predictions that can be found in the literature for the same setup, see Fig. 6b. The comparison is generally found to be good where the presented results are particularly consistent with the simulation results of Apte et al. [2] and Breugem [4]. At this point, one has to underline that all predicted evolutions in Fig. 6b rely on different FD method concepts.

In Fig. 7, the process of *drafting-kissing-tumbling* is displayed at eight different points in time. One observes that once the trailing particle is located within the gradually growing wake region of the leading particle, it experiences a lower drag force. Consequently, this results in a higher fall velocity for the trailing particle compared to the leading particle (drafting). With increasing time, the gap between both particles decreases due to their velocity difference, and thus the particles get—after a while—into contact (kissing). Clearly, this configuration is unstable. The particles tumble as a consequence and start to separate (tumbling). The flow phenomena observed in the experiment of Fortes et al. [15] are definitely reproduced by the presented computational approach.

6.3 Particle-Laden Flow Through a Tube

In this test case, a particle-laden flow through a tube with different cross sections is considered. It is assumed that the particles are allowed to adhere to each other and as
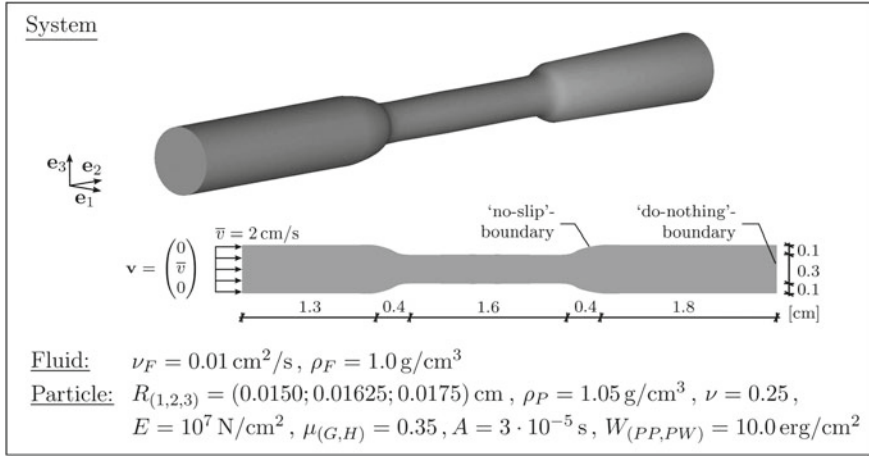
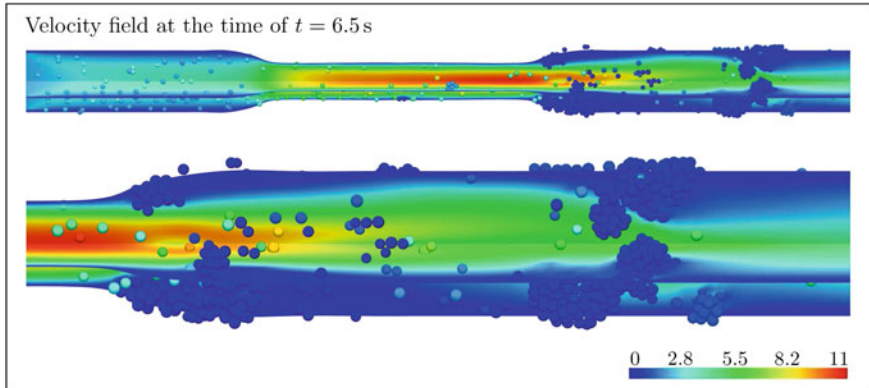**Fig. 8** Particle-laden flow through a tube. Geometry and material data

Fig. 9 Numerical results of the flow through the tube showing the velocity field at $t = 6.5$ [s]

well at the tube wall. Figure 8 shows the geometry of the tube including the model data, where the parameters W_{PP} and W_{PW} are the work of adhesion among particles and between particles and the tube wall, respectively. Gravitational effects are not considered. The suspended particles are randomly inserted at the inflow boundary with an initial velocity which is conform to the inflow velocity of the fluid. To compute the flow in the tube, a mesh consisting of 2,304,000 $\tilde{Q}_1/Q_0$ elements is used. This yields a discretized system with 2,304,000 pressure nodes and 6,953,280 velocity nodes. The time step sizes for the FEM and DEM solver are selected as $\Delta t = 10^{-4}$ s and $\Delta t_D = 10^{-6}$ s, respectively.

The presence of van der Waals forces leads with the chosen parameters to a deposition of suspended particles onto the tube wall. The deposition grows with an increasing simulation time, in particular at the end of the smaller cross section
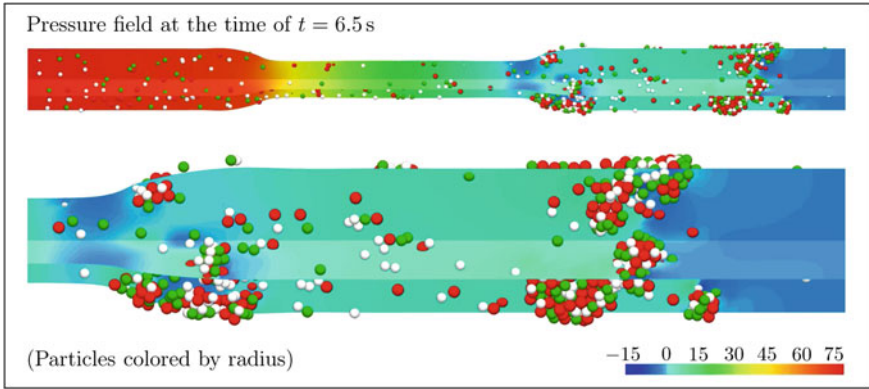
Fig. 10 Numerical results of the flow through the tube showing the pressure field at $t = 6.5$ [s]
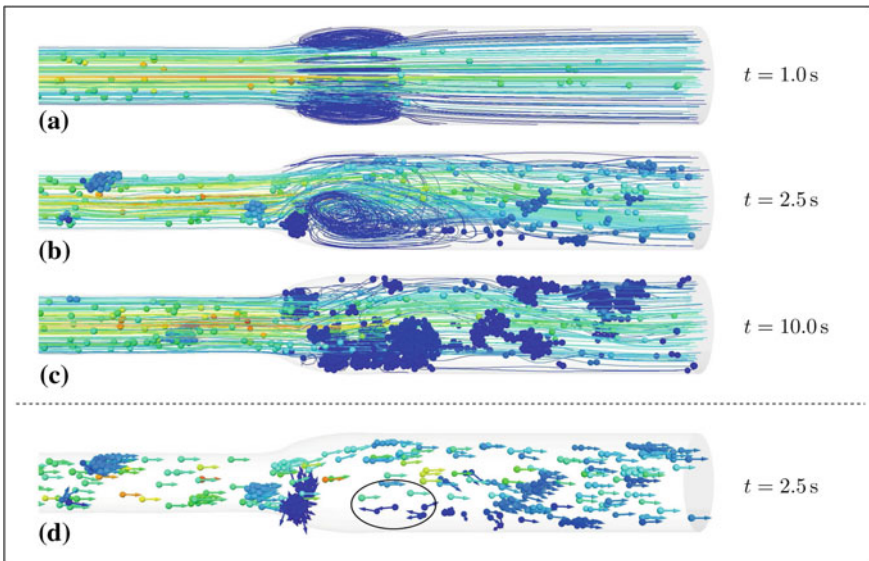

Fig. 11 Numerical results of the flow through the tube showing: **a–c** the streamlines and the particles at different points in time and **d** the particle velocity vectors at $t = 2.5$ s. The *colors* represent in all cases the velocity magnitudes

part. With more particles adhering to the wall, the velocity increases locally, and the particles experience higher drag forces. A situation like this is depicted in Fig. 9. Therein, one can see the influence of the developed agglomerates on the velocity field when they stick to the tube wall or slide along the wall. Due to the fully coupled description of the particulate flow, the strong mutual phase interactions, as in the situation shown in Fig. 9, can be captured by the developed DNS fluid-particle solver. The strong local impact of the dispersed phase on the fluid phase is here
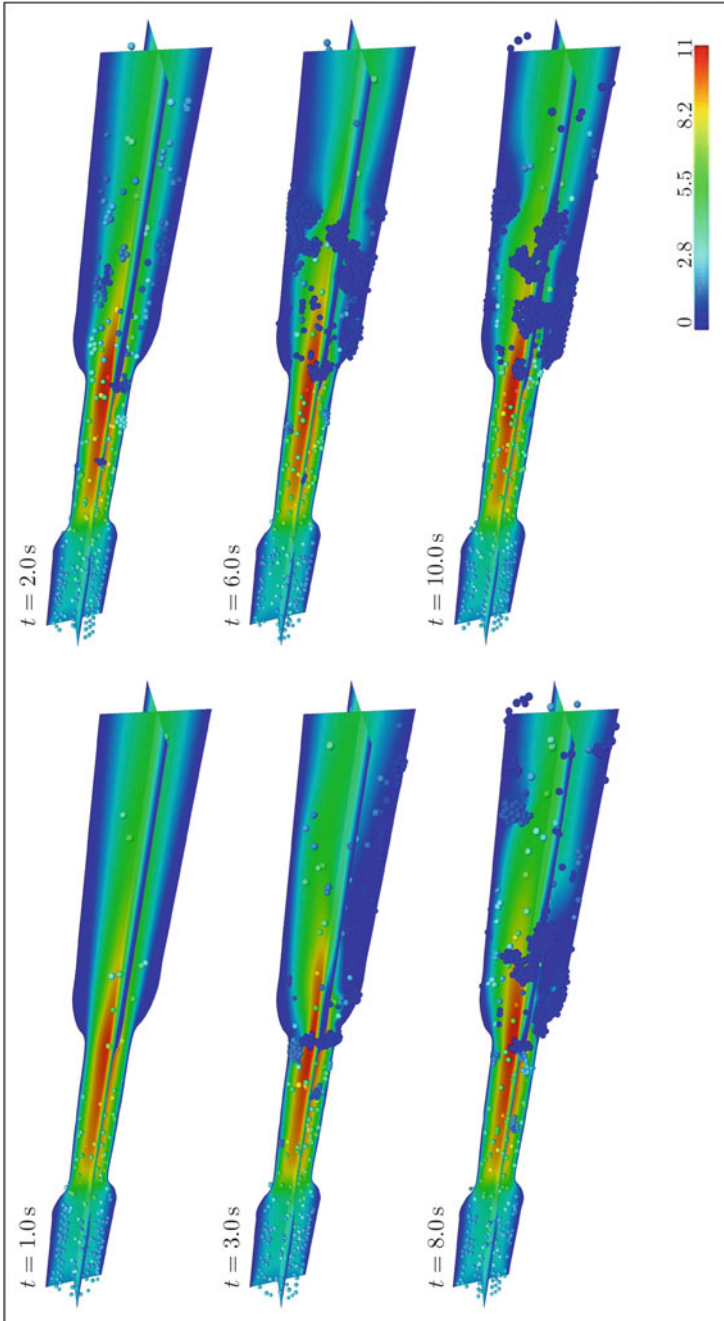
Fig. 12 Numerical results of the flow through the tube showing the fluid and particle velocities at six points in time

obvious. In Fig. 10, one can observe the corresponding effects regarding the pressure field (see the pressure difference when comparing the luv and the lee side of the large agglomerate). For the case when the traction forces exceed the adhesive forces, single particles and agglomerates break off and are subsequently transported away by the flow field. The complexity of the evolution of the multiphase flow situation at the outflow of the smaller cross section part is reflected in Fig. 11. There, the image (a), which shows the flow at time $t = 1.0$ s, illustrates a fully developed axisymmetric fluid flow with a certain eddy zone evolved in this region. Having a look at the images (b) and (c), $t = 2.5$ s and $t = 10.0$ s, one can see that this axial symmetry is totally lost and that a large number of particles has deposited on the wall. The image (d) shows the same flow situation as in (b), but in this case including particle velocity vectors and without streamlines. Here, the influence of the eddy on the trajectories of the passing particles can be clearly seen. In fact, the particles which are fully caught by the eddy change the flow direction so that they are subsequently transported against the main flow in the tube. The different phases of the flow process are shown for the whole system in Fig. 12.

7 Conclusion

In this work, a computational approach for the full 3D DNS of particulate flows is presented. The approach is based on the FD method. The developed solver treats the coupled fluid-particle problem in a staggered way by solving the phases explicitly in succession. The mutual phase interactions are computed on the other hand implicitly. As numerical solvers, the FEM and DEM are applied, respectively, to simulate the fluid and particle part. In the framework of the DEM, the particle collision is described using an adhesive viscoelastic model, and additionally, friction and rolling resistance are considered. To verify the reliability of the algorithm and its implementation, various test computations were performed. In this contribution, the simulation results of two sedimentation problems were presented and discussed. Furthermore, the solver was applied to simulate an aggregation dynamics problem of a particulate flow where the formation of agglomerates is considered. The chosen system for this task was a tube with different cross sections. The obtained numerical results show that the developed solver is appropriate to deal with fluid-particle interaction problems.

References

1. Allen MP, Tildesley DJ (1987) Computer simulation of liquids. Oxford University Press, New York
2. Apte SV, Martin M, Patankar NA (2009) A numerical method for fully resolved simulation (FRS) of rigid particle-flow interactions in complex flows. J Comput Phys 228(8):2712–2738
3. Avci B, Wriggers P (2012) A DEM-FEM coupling approach for the direct numerical simulation of 3D particulate flows. J Appl Mech 79:010901

4. Breugem WP (2012) A second-order accurate immersed boundary method for fully resolved simulations of particle-laden flows. J Comput Phys 231(13):4469–4498
5. Brilliantov NV, Albers N, Spahn F, Pöschel T (2007) Collision dynamics of granular particles with adhesion. Phys Rev E 76(5, Part 1):051302
6. Brilliantov NV, Spahn F, Hertzsch JM, Pöschel T (1996) Model for collisions in granular gases. Phys Rev E 53(5, Part B):5382–5392
7. Brown PP, Lawler DF (2003) Sphere drag and settling velocity revisited. J Environ Eng 129(3):222–231
8. Cheng NS (2009) Comparison of formulas for drag coefficient and settling velocity of spherical particles. Powder Technol 189(3):395–398
9. Chokshi A, Tielens AGGM, Hollenbach D (1993) Dust coagulation. Astrophys J 407(2, Part 1):806–819
10. Clift R, Grace JR, Weber ME (1978) Bubbles, drops and particles. Academic Press, New York
11. Crowe CT (2006) Multiphase flow handbook. CRC Press, Boca Raton
12. Cundall PA, Strack ODL (1979) Discrete numerical model for granular assemblies. Geotechnique 29(1):47–65
13. Feng YT, Han K, Owen DRJ (2007) Coupled lattice Boltzmann method and discrete element modelling of particle transport in turbulent fluid flows: computational issues. Int J Numer Meth Eng 72(9):1111–1134
14. Feng ZG, Michaelides EE (2005) Proteus: a direct forcing method in the simulations of particulate flows. J Comput Phys 202(1):20–51
15. Fortes AF, Joseph DD, Lundgren TS (1987) Nonlinear mechanics of fluidization of beds of spherical-particles. J Fluid Mech 177:467–483
16. Glowinski R, Pan TW, Hesla TI, Joseph DD, Periaux J (2001) A fictitious domain approach to the direct numerical simulation of incompressible viscous flow past moving rigid bodies: application to particulate flow. J Comput Phys 169(2):363–426
17. Haeri S, Shrimpton JS (2012) On the application of immersed boundary, fictitious domain and body-conformal mesh methods to many particle multiphase flows. Int J Multiph Flow 40:38–55
18. Hertz H (1882) Über die berührung fester elastischer körper. Journal für die reine und angewandte Mathematik 92:156–171
19. Hu HH (1996) Direct simulation of flows of solid-liquid mixtures. Int J Multiph Flow 22(2):335–352
20. Hu HH, Joseph DD, Crochet MJ (1992) Direct simulation of fluid particle motions. Theor Comput Fluid Dyn 3:285–306
21. Hu HH, Patankar NA, Zhu MY (2001) Direct numerical simulations of fluid-solid systems using the Arbitrary Lagrangian-Eulerian technique. J Comput Phys 169(2):427–462
22. Iwashita K, Oda M (1998) Rolling resistance at contacts in simulation of shear band development by DEM. J Eng Mech 124(3):285–292
23. Johnson AA, Tezduyar TE (1996) Simulation of multiple spheres falling in a liquid-filled tube. Comput Methods Appl Mech Eng 134(3–4):351–373
24. Johnson AA, Tezduyar TE (1997) 3D simulation of fluid-particle interactions with the number of particles reaching 100. Comput Methods Appl Mech Eng 145(3–4):301–321
25. Johnson AA, Tezduyar TE (1999) Advanced mesh generation and update methods for 3D flow simulations. Comput Mech 23(2):130–143
26. Johnson AA, Tezduyar TE (2001) Methods for 3D computation of fluid-object interactions in spatially periodic flows. Comput Methods Appl Mech Eng 190(24–25):3201–3221
27. Johnson KL, Kendall K, Roberts AD (1971) Surface energy and contact of elastic solids. Proc R Soc Lond A 324(1558):301–313
28. Kruggel-Emden H, Wirtz S, Scherer V (2008) A study on tangential force laws applicable to the discrete element method (DEM) for materials with viscoelastic or plastic behavior. Chem Eng Sci 63(6):1523–1541
29. Kuhn MR, Bagi K (2004) Alternative definition of particle rolling in a granular assembly. J Eng Mech 130(7):826–835

30. Lebedev VI, Laikov DN (1999) Quadrature formula for the sphere of 131-th algebraic order of accuracy. Dokl Akad Nauk SSSR 366(6):741–745
31. Loskofsky C, Song F, Newby BZ (2006) Underwater adhesion measurements using the JKR technique. J Adhes 82(7):713–730
32. Luding S (2004) Micro-macro transition for anisotropic, frictional granular packings. Int J Solids Struct 41(21):5821–5836
33. Luding S (2008) Cohesive, frictional powders: contact models for tension. Granular Matter 10(4):235–246
34. Luo K, Wang Z, Fan J (2007) A modified immersed boundary method for simulations of fluid-particle interactions. Comput Methods Appl Mech Eng 197(1–4):36–46
35. Maugis D (1992) Adhesion of spheres—the JKR-DMT transition using a Dugdale model. J Colloid Interface Sci 150(1):243–269
36. Pöschel T, Schwager T (2005) Computational granular dynamics. Springer, New York
37. ten Cate A, Nieuwstad CH, Derksen JJ, van den Akker A (2002) Particle imaging velocimetry experiments and lattice-Boltzmann simulations on a single sphere settling under gravity. Phys Fluids 14(11):4012–4025
38. Turek S (1999) Efficient solvers for incompressible flow problems: an algorithmic and computational approach. Springer, Berlin
39. Turek S, Becker C (1998) FEATFLOW. Finite element software for the incompressible Navier-Stokes equations. Institute for Applied Mathematics, University of Heidelberg, Heidelberg
40. Veeramani C, Minev PD, Nandakumar K (2007) A fictitious domain formulation for flows with rigid particles: a non-lagrange multiplier version. J Comput Phys 224(2):867–879
41. Wachs A (2009) A DEM-DLM/FD method for direct numerical simulation of particulate flows: sedimentation of polygonal isometric particles in a Newtonian fluid with collisions. Comput Fluids 38(8):1608–1628
42. Wan D, Turek S (2006) Direct numerical simulation of particulate flow via multigrid FEM techniques and the fictitious boundary method. Int J Numer Meth Fluids 51(5):531–566
43. Wriggers P (2006) Computational contact mechanics, 2nd edn. Springer, Berlin